Simultaneous photoactivation and high-speed structural tracking reveal diffusion-dominated motion in the endoplasmic reticulum

Matteo Dora,[1,*] Christopher J. Obara,[2,*] Tim Abel,[3,4] Jennifer Lippincott-Schwarz,[2] and David Holcman[1,5,†]

[1] *IBENS, École Normale Supérieure PSL, 75005 Paris, France*
[2] *Janelia Research Campus, Howard Hughes Medical Institute, Ashburn, Virginia 20147 USA*
[3] *Max-Delbrück Center for Molecular Medicine, Robert-Rössle Strasse 10, 13092 Berlin, Germany.*
[4] *Institut für Biologie/Molekulare Biophysik, Humboldt-Universität zu Berlin, Germany.*
[5] *DAMPT, University of Cambridge and Churchill College, CB30DS Cambridge, UK*

(Dated: 23rd April 2023)

The endoplasmic reticulum (ER) is a structurally complex, membrane-enclosed compartment that stretches from the nuclear envelope to the extreme periphery of eukaryotic cells. The organelle is crucial for numerous distinct cellular processes, but how these processes are spatially regulated within the structure is unclear. Traditional imaging-based approaches to understanding protein dynamics within the organelle are limited by the convoluted structure and rapid movement of molecular components. Here, we introduce a combinatorial imaging and machine learning-assisted image analysis approach to track the motion of photoactivated proteins within the ER of live cells. We find that simultaneous knowledge of the underlying ER structure is required to accurately analyze fluorescently-tagged protein redistribution, and after appropriate structural calibration we see all proteins assayed show signatures of Brownian diffusion-dominated motion over micron spatial scales. Remarkably, we find that in some cells the ER structure can be explored in a highly asymmetric manner, likely as a result of uneven connectivity within the organelle. This remains true independently of the size, topology, or folding state of the fluorescently-tagged molecules, suggesting a potential role for ER connectivity in driving spatially regulated biology in eukaryotes.

I. INTRODUCTION

One of the most notable aspects of eukaryotic life is the development of membrane-enclosed organelles [5]. These compartments provide two important advantages to cells. First, they segregate unique chemical environments that allow incompatible biochemical reactions to occur simultaneously, and second, they provide extensive two-dimensional surfaces (membranes) to facilitate the efficiency of biological reactions [2]. The largest organelle in eukaryotes is the endoplasmic reticulum (ER). It is a major site of cellular translation, protein folding, and quality control [50, 51], the major cellular calcium store and sink in most cells [7], and the primary site of lipid synthesis and regulation [66]. In addition to these crucial cellular functions, it also makes contact with and regulates the biology of essentially every other cellular compartment through specific tethering molecules [49]. Thus, understanding how molecules are spatially distributed over time within the ER network is important for understanding how their functions are achieved.

Topologically, the ER is a single, immense compartment that divides the nucleoplasm from the cytoplasm and stretches to the furthest reaches of the cell as a structurally complex membrane-enclosed network [21]. It remains a fundamental question how biological phenomena are spatially coordinated within the network, since there are no known ER-localized structural proteins or motors.

The development of technologies for fluorescent tagging of molecules has opened the possibility to probe the dynamic nature of proteins within the ER [14, 64]. In particular, FRAP and FLIP [33] have provided significant insight into the way many components of the compartment behave [35]. These studies have suggested that the composition of the organelle is strikingly dynamic, equilibrating on a timescale of seconds [10, 42]. However, these studies are limited to timescales of tens of seconds to minutes (FLIP) or single structurally heterogeneous spatial regions (FRAP), and the ability to simultaneously observe high-speed ensemble dynamics across the entire cell has proven elusive. The development of photoactivatable fluorophores [48] has allowed this type of experiment in other systems [26, 44], but most photoactivatable fluorophores do not fold correctly or provide low SNR in the high redox environment of the ER lumen [11, 29].

An additional limitation to understanding protein redistribution within the ER is provided by the convoluted structure of the organelle itself [61]. The small size of ER substructures necessitates that molecules are not free to move uniformly in any dimension. Previous work has attempted to account for this with a number of clever modeling-based approaches, but the inability to directly observe the structure in question during fluorescent recovery has led to inconsistent results from varying model assumptions [46, 54, 55, 58].

In this article, we develop a combined experimental and analysis pipeline to surmount these two issues. We have used photoactivation of protein-linked organic dyes that work well within the ER lumen to track the dynamic distribution of ER-localized molecules. During photoactivation and imaging, we simultaneously image the underlying structure of the organelle with an independent camera and orthogonal fluorescent label. This approach supports high speed imaging while also collecting entire cells, and allows us to place the photoactivated material back in the structure it is localized to in real time. We then coupled this to a novel, ma-

* Contributed equally.
† david.holcman@ens.psl.eu

chine learning-assisted analysis pipeline to provide a first-order approximation of the complex organelle structure, allowing estimation of the potential paths taken by the fluorescent components. Collectively, this pipeline allows the extraction of quantitative information about the molecular behaviour within the ER at the whole-cell scale.

II. RESULTS

In order to track ER protein dynamics across entire cells, we utilized photoactivatable organic dyes that can be directly coupled to a protein of interest by genetic fusion to a HaloTag [15, 22, 36]. These dyes are functional in the ER lumen and do not induce the misfolding and ER stress-related pathways common with fluorescent proteins not optimized for the high redox environment within this compartment [12]. Once labelled with the dye, proteins of interest can be fluorescently marked at specific locations within the ER structure, and their distribution over time can be monitored by high speed microscopy. We performed experiments in cells also expressing a non-perturbative GFP-derivative targeted to the ER lumen [11], to provide a simultaneously collected map of the underlying structure of the ER for downstream analysis purposes.

Briefly, COS-7 cells were cotransfected with a GFP-derivative targeted to the ER lumen to label the structure and a HaloTag fused to the protein construct of interest. We then used high speed spinning disk microscopy (at 10 Hz acquisition rate) using dual cameras to simultaneously collect the distribution of the photoactivated species of the dye and the fluorescence of the GFP label, resulting in two stacks of 2D images at 100 ms intervals. Photoactivation was carried out continuously at single, diffraction limited spot, and the diffusion of molecules away from that spot was visible in the distribution of the converted dye molecule.

A. Ensemble diffusion governs dynamics of ER luminal content

We first set out to evaluate the dynamics of lumen-resident proteins that are freely floating (i.e. without membrane anchors or known specific binding partners). We assumed a globally isotropic but not necessarily diffusive motion, since local directional flows may be present [27]. We used a HaloTag targeted to the ER lumen with a signal sequence and a KDEL retention motif as a model probe for free-floating luminal content (HaloTag–KDEL). Photoactivation was carried out at a single point (PA source) while simultaneously collecting both the GFP-labeled ER structure and the photoactivated signal using dual camera spinning disk microscopy (fig. 1A).

Proteins within the ER lumen are constrained to compartment by the bounding membrane, so they are not free to move in any arbitrary direction. Thus, analysis of the distribution patterns must account for the underlying organelle structure, or model fitting will produce artefacts [60]. To address this, we first segmented the ER by analysing the GFP channel to extract the network structure (see *Methods*, section IV A and supplementary figure S1). Regions of the ER were characterized by their distance from the PA source as measured through the underlying structure of ER (fig. 1A, inset), as opposed to Euclidean distance (fig. 1A, dashed line).

Using this approach, the estimated arrival time of fluorescent molecules can be coupled with the distance from the PA source and the amount of photoactivation to produce an effective diffusion model. In principle, this model depends on the rate of photoconversion by the photoactivation laser, which cannot be easily determined. To circumvent this issue, we take a hybrid data-driven modelling approach. We first quantified the photoactivated fluorescence over time at the PA source and fitted it with an arbitrary parametric function $\phi(t)$. In our case, we found that a function $\phi(t)$ in the form of a sum of saturating exponentials could well describe the data (fig. 1B1, and see *Methods*). We then fixed the effective diffusion model conditioning it on $\phi(t)$ at the source region, effectively constraining the model based on the measured intensity of the PA source. Once the source parameters were determined, we performed a maximum-likelihood fit of the fluorescence intensity model to extract the effective diffusion coefficients corresponding to the average fluorescence measured in the equidistant points (fig. 1B2). We constrained the model parameters based on the density of the ER structure which we estimated from the GFP channel (*Methods*, section IV C). The fluorescence intensity model also considers the possible background photoactivation (fig. 1B2, dashed line) due to inefficient photoactivation of the dye by the laser used to image the GFP. Note that this approach can be modified to deal with sources of anisotropy if the model fit is not good, as would be predicted by synchronous directed flows or other micron scale sources of anisotropy (see below). We then repeated this procedure for every distance value in the structure, obtaining distance-dependent estimations of the effective diffusion coefficient. In fig. 1C we compare, on an example cell, the results of this morphology-aware model (orange) to a standard maximum-likelihood fit that only considers Euclidean distances and that does not impose constraints based on ER density (light blue). We note that the approach that does not take ER morphology into account produces estimates of the diffusion coefficient that increase with the distance from the PA source (an indication of super-diffusive motion), while such effect disappears when considering a morphology-aware model.

In the immediate proximity of the PA source both approaches are highly sensitive to variations in fluorescence and can badly estimate the effective diffusion coefficient. Similarly, the quality of the fit degrades in regions that are too far away from the PA source, since only a relatively small fraction of molecules can reach those regions over the considered timescale, thus decreasing the signal-to-noise ratio of the measured fluorescence. To mitigate these issues, we estimate the uncertainty of the diffusion coefficient fit based on observed Fisher information (see *Methods*, section IV C), discarding data points with standard deviation above a threshold of $0.1\,\mu m^2\,s^{-1}$. We then defined a characteristic effective diffusion coefficient for each cell by considering the median value of the valid diffusion estimates.

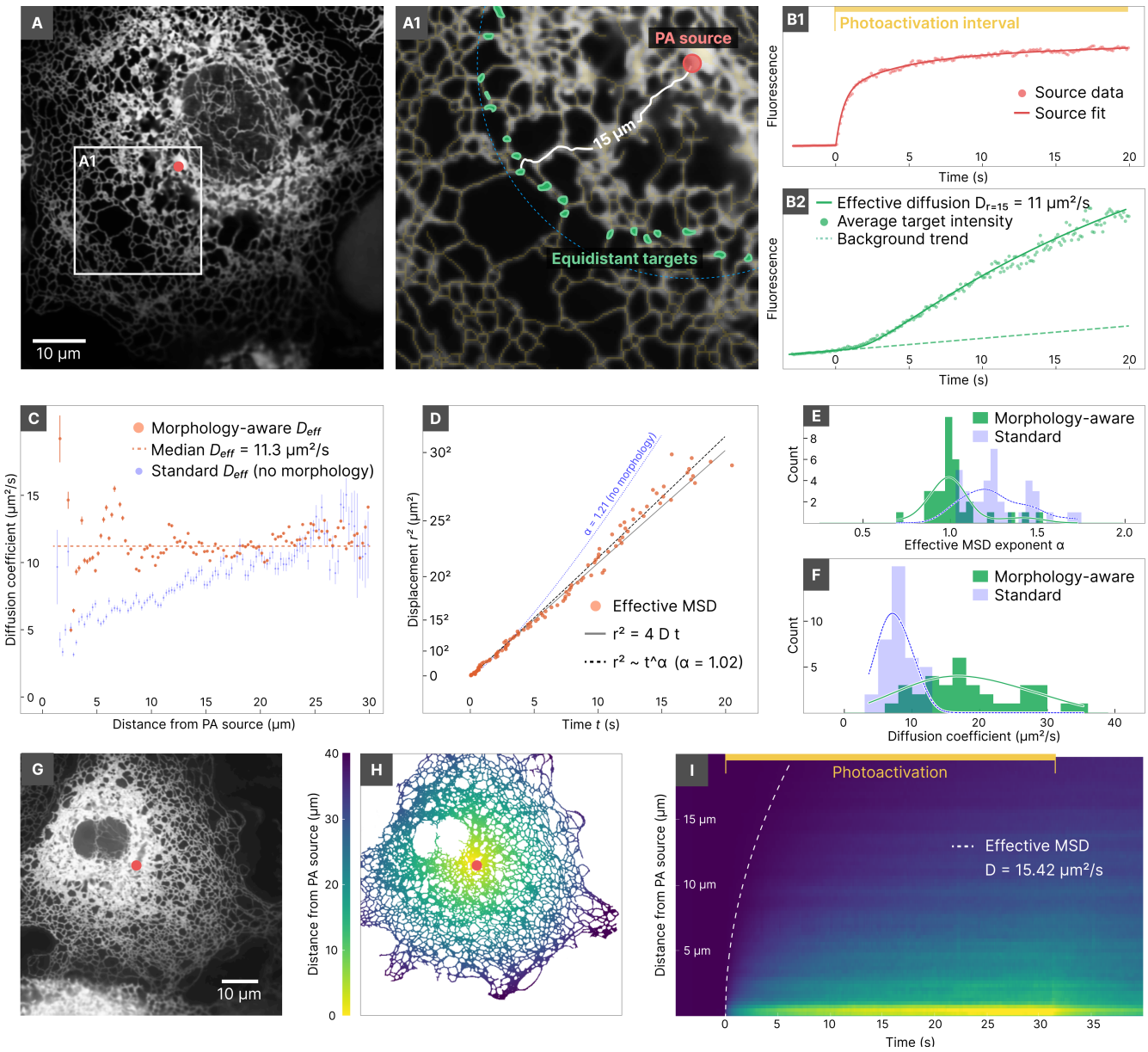

Figure 1. **Brownian diffusion governs large scale ER luminal dynamics.** **A** The ER structure of a COS-7 cell. The red dot indicates the location of photoactivation. Green regions correspond to ER domains that are equidistant (d = 15 µm) from the photoactivation region (distance calculated the ER morphology). The blue dashed line denotes the Euclidean distance of 15 µm from the photoactivation region when the ER morphology is neglected. **B1** Data and analytical fit of the fluorescence curve inside the photoactivation region. **B2** Average fluorescence of the target regions at distance 15 µm from the photoactivation source and fit of effective diffusion model (D = 11 $\mu m^2\, s^{-1}$). **C** Effective diffusion coefficient as a function of the distance d from the photoactivation region, obtained from separate fits at each distance, for the morphology-aware model (orange) and the standard model neglecting ER morphology (light blue). The error bars represent the approximated confidence interval estimated by observed Fisher information (± 5 standard deviations). **D** Effective mean-squared displacement (MSD) obtained by ensemble estimate. **E** Distribution of the effective MSD exponent α of each cell for the morphology-aware and the standard model (N = 33 and N = 37 respectively), obtained by ensemble estimate. **F** Distribution of the median cellular diffusion coefficients obtained by ensemble estimate for HaloTag–KDEL in the ER lumen, comparing the morphology-aware model (green) and the standard model neglecting morphology (light blue). **G** Example of ER in a COS-7 cell. The photoactivation region is denoted by the red dot. **H** Structure of the ER network of the cell in G with colour scale denoting distances from the photoactivation source. **I** Kymograph of the average fluorescence in time of the cell in G, binned over the distance from the photoactivation source through the structure. The white dashed line denotes the squared root of effective MSD curve of the diffusion model that was fit ($d = \sqrt{4D_{\text{eff}}t}$).

We found for the HaloTag–KDEL condition a population diffusion coefficient $16.84\,\mu m^2\,s^{-1}$ (fig. 1F), which is very similar to previously reported estimates based on FRAP and SPT [27, 42, 59].

To evaluate the validity of a diffusion model more generally, we represented the fit results for each cell in the form of effective diffusion timescales, creating an effective MSD curve describing the time evolution of the average distance travelled by a protein released from the PA source (fig. 1D). The exponent α of the MSD curve allowed us to evaluate possible deviations from standard diffusion ($\alpha = 1$) such as subdiffusion ($\alpha < 1$) or superdiffusion ($\alpha > 1$). For each cell, we determined the MSD exponent α by fitting the effective MSD data with $c\,t^{\alpha}$ (fig. 1D), comparing the proposed morphology-aware model (black dashed line) with the MSD obtained from a standard model that neglects ER morphology (blue dotted line). We found that population statistics of HaloTag–KDEL condition had an average MSD exponent $\alpha \approx 1$, thus suggesting that luminal dynamics can be well described by standard diffusion over this spatiotemporal scale (fig. 1E, green). We also note how neglecting ER morphology resulted in apparent super-diffusive behaviour with $\alpha > 1$ (fig. 1E, light blue).

For organelles with less complex morphology, changes in the distribution of fluorescent molecules over time are often effectively represented with a kymograph, i.e. a time-space plot of the fluorescence observed along one dimension over time [28, 38, 73]. In the ER, this is challenging due to the circuitous and dynamic nature of paths through the structure and the relatively low number of fluorescent molecules present in any isolated structural component. As a visualization tool, we used the distances calculated between the PA source and every point of the segmented ER structure (fig. 1G–H), and averaged the fluorescence values at each distance to create an equivalent kymograph describing the time-evolution of the fluorescence as a function of the distance from the PA source (fig. 1I). This representation shows concentrated photoactivated signal at the bottom (close to the PA source) and a gradual spreading through the structure moving upwards (towards distant regions) as the time of photoactivation increases. As a qualitative evaluation of the diffusion model fit to this cell, the time evolution of the fluorescence is well contained within the bounds predicted by pure diffusion at this effective diffusion coefficient.

To qualitatively confirm that our approach is appropriate, we simulated purely diffusive motion on the experimentally-obtained ER morphology by evaluating the proposed effective diffusion model with constant diffusion coefficient defined as the median of the maximum-likelihood fit for a cell (see *Methods*, section IV C). We then blended the result with the GFP-labeled channel to reproduce the inhomogeneous density of the ER structure. We found that the simulated distribution could qualitatively reproduce the experimental photoactivation data with reasonable fidelity, suggesting that pure diffusion models are a good fit for ER luminal content at this spatiotemporal scale (fig. 1). This suggests that a large part of the heterogeneity observed in the photoactivated channel is due to the varying density of the underlying ER structure and not to uneven mixing of the molecules (fig. 1B).

B. Heterogeneity in apparent luminal mixing dynamics

The data presented thus far is analysed assuming a reasonable degree of isotropy in the system, since locations at similar distances from the PA source are averaged together. While this approach generally fits the data well, we observed cells where the fit of the model was poor due to apparent anisotropy in the mean arrival times of fluorescent proteins.

To evaluate this heterogeneity, we decided to perform a spatially resolved model fit weighted by the amount of ER structure present. We first subdivided the field of view with a square grid of size 400 nm (fig. 3A). We then calculated the average fluorescence of the segmented ER portion contained in each grid bin for each frame in the temporal stack (fig. 3B). We discarded bins which did not contain ER structure for at least half of the time frames. We thus obtained a time evolution curve of the photoactivated fluorescence for each non-empty bin (fig. 3C). After fixing the PA source parameters as described above, we estimated an effective diffusion coefficient for each grid bin (see *Methods*, section IV C), obtaining spatial maps of the effective diffusion coefficients (fig. 3D). Regions characterized by higher diffusion coefficients are associated with faster arrival of luminal proteins. We observed occasional cases of strong local heterogeneity in the dispersal of fluorescent proteins, represented by regions exhibiting faster arrival time with respect to the cell median mixing time (fig. 3D). Such regions seem to be localized in denser perinuclear regions of the ER, close to the nuclear envelope.

To ascertain whether this heterogeneity could be explained by an increased reshaping of the ER morphology in the affected regions, we quantified the morphology variation and tubule motion (see *Methods*, section IV A and supplementary figure S2). We found no association between higher morphological reshaping and regions with increased mixing dynamics, suggesting that motion of the ER structure is unlikely to be the source of the observed anisotropy in the redistribution timescales.

Despite the variation in mean arrival times of fluorescent proteins, these cells still did not have MSD coefficients significantly different from 1 when considering the full cell data. Thus, this heterogeneity is likely to have to do with uneven connectivity within the structure rather than large scale directed motion (see *Discussion*). This is consistent with recently published three-dimensional electron microscopy volumes, showing significant variation in the mean luminal cross-section size in the perinuclear region of some cells [25].

C. Effects of membrane anchoring on ER protein diffusion

Early work in the literature showed that viscous drag of domains anchored in membranes is much higher than the drag on soluble domains. Consequently, membrane proteins

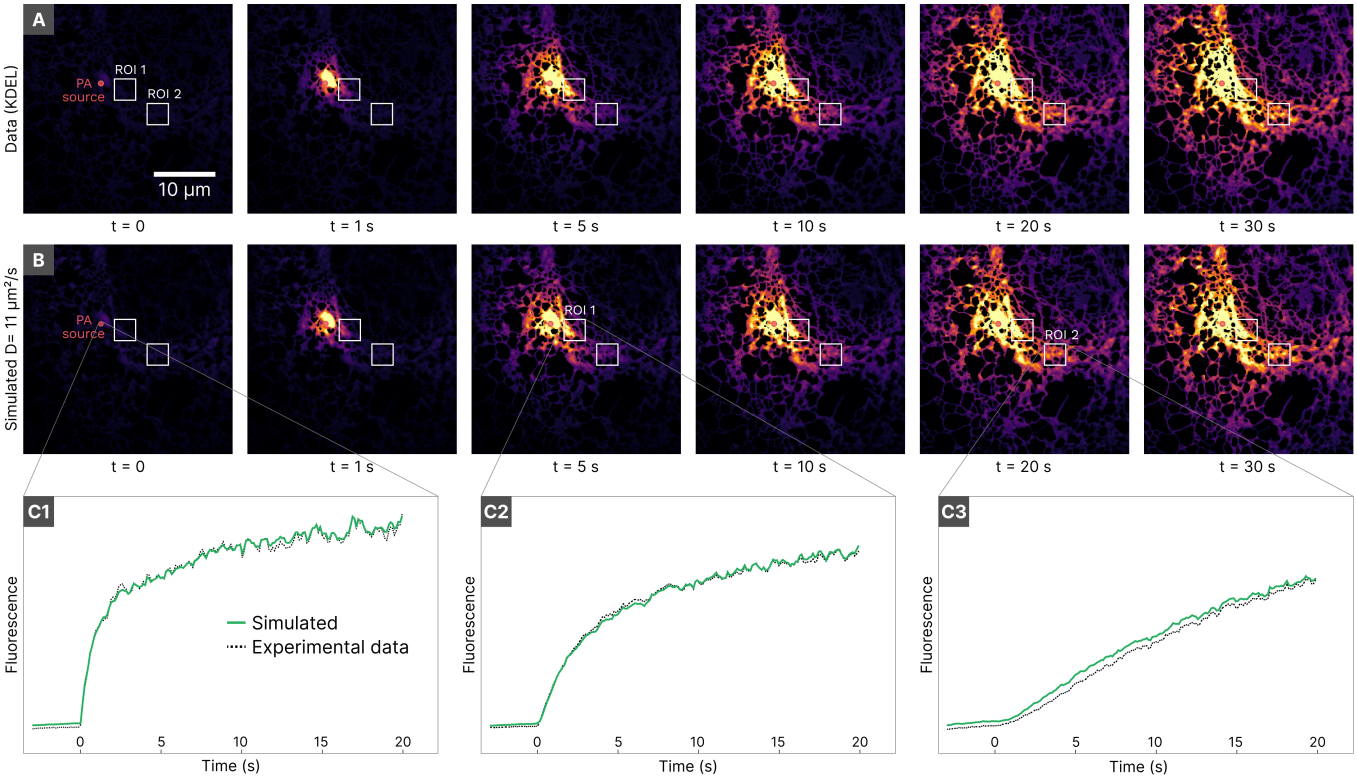

Figure 2. **A** Experimental snapshots at different time intervals from the beginning of photoactivation. **B** Simulated snapshots built by evaluating the effective diffusion model on the ER shape obtained by experimental data, using the median diffusion coefficient obtained by the morphology-aware maximum-likelihood fit. **C** Comparison of experimental and simulated fluorescence curves at the photoactivation source (C1) and at two ROIs (C2 and C3) located at different distances from the PA source.

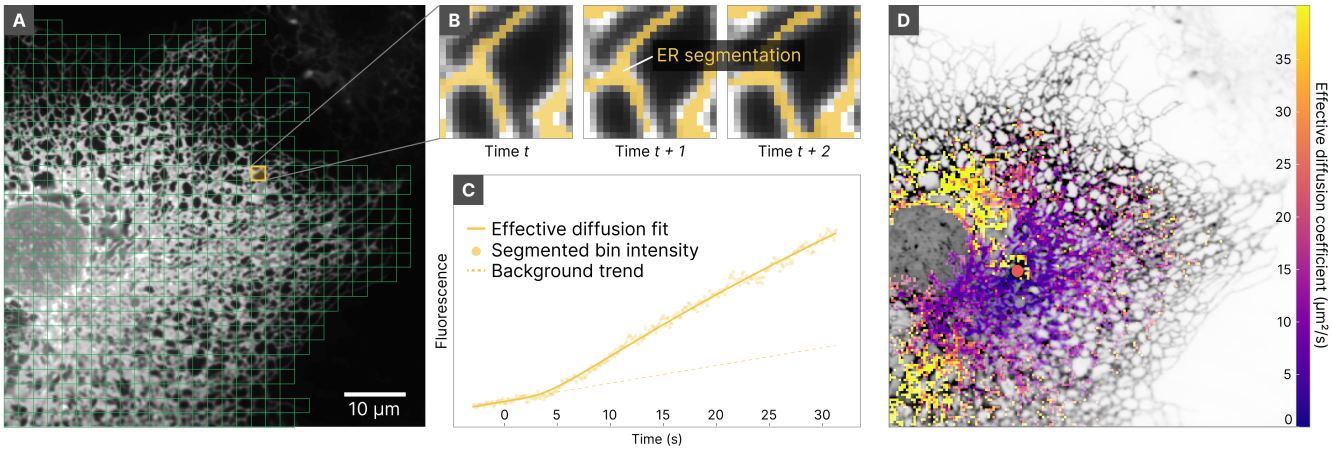

Figure 3. **Heterogeneity in luminal mixing dynamics.** **A** Subdivision of the ER using a grid of square bins. (A large bin size is used for easier visualization.) **B** An example of ER-associated, segmented pixels belonging to a given bin as they are tracked through time. **C** Average fluorescence over time for segmented pixels belonging to the bin shown in B. Dotted line shows the model fit. **D** Example of spatial map describing the observed mean arrival time, represented by a space-dependent effective diffusion coefficient (higher is faster). The red dot indicates the PA source. The grid bin size is 400 nm (3×3 camera pixels).

generally show significantly lower effective diffusion coefficients than proteins freely floating within the lumen [34]. To examine the effect of this in our system, we compared the diffusion of HaloTag freely floating in the ER lumen (HaloTag–KDEL condition) and the same HaloTag anchored to the ER membrane (HaloTag–Sec61β condition). The membrane anchoring was achieved by fusing HaloTag genetically to a minimal membrane targeting domain from Sec61β that is known not to interact with the translocon in living cells [45].

We evaluated both space-dependent and isotropic diffu-

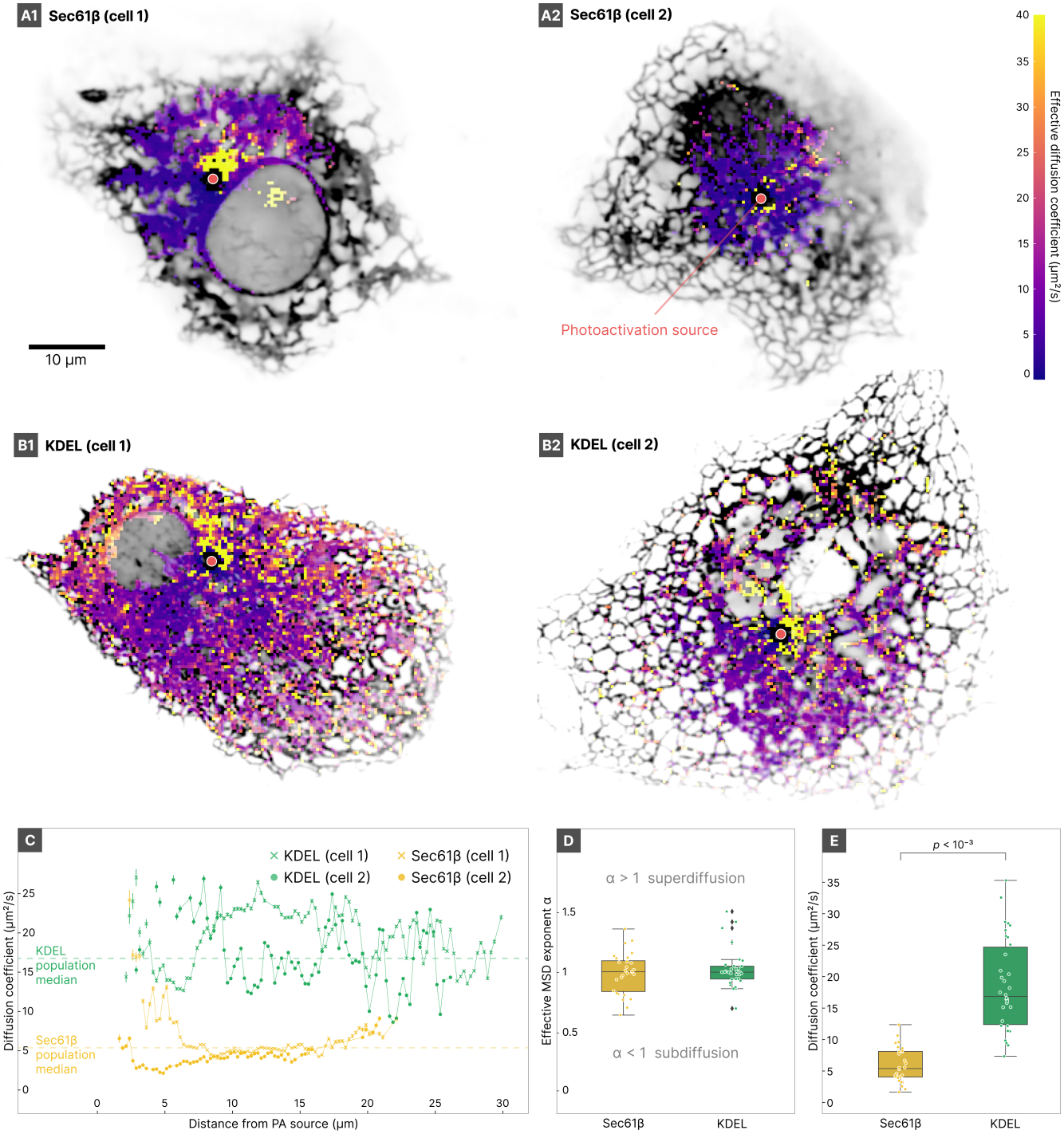

Figure 4. **Comparison of ER protein dynamics in the lumen and in the membrane.** **A** Examples of spatial diffusion map for HaloTag-Sec61β. **B** Representative examples of the spatial diffusion map of HaloTag–KDEL. **C** Results for the isotropic diffusion fit (averaged over all targets at fixed distance) for cells A1–2 and B1–2. **D** Population statistics of the effective MSD exponent of HaloTag–KDEL and HaloTag-Sec61β conditions. **E** Population statistics of the effective diffusion coefficient D_{eff} of HaloTag–KDEL and HaloTag-Sec61β conditions.

sion coefficients under both conditions. We found no significant difference between the two conditions regarding heterogeneity of the mixing dynamics, which were at least qualitatively comparable and isotropic in the majority of cells (e.g. fig. 4A1–A2,B1–B2). However, in agreement with the literature, the HaloTag–Sec61β moved significantly less far through the structure for the same acquisition time (fig. 4A–B). As a result, spatial diffusion maps for the HaloTag–Sec61β condition could typically only be evaluated in a smaller region around the PA source (up to 15 µm), where the SNR was suf-

ficiently high with respect to the baseline. Estimation of the isotropic diffusion characteristics was consistent with published literature [60] and the previous results with HaloTag–KDEL (fig. 4C), showing that membrane dynamics was well described by standard Brownian diffusion (MSD exponent $\alpha = 1.02$, fig. 4D). Population level statistics for the effective diffusion coefficient (fig. 4D) confirmed that membrane proteins are diffusing significantly slower than luminal proteins in our system (membrane $D_{\text{Sec61}\beta}$ = 5.39 μm^2 s^{-1}, compared to luminal D_{KDEL} = 16.84 μm^2 s^{-1}, p-value < 1 × 10^{-3}).

D. Effect of protein size on mixing dynamics

Since the drag of a transmembrane anchor had such a dramatic effect on the apparent diffusion of molecules in the ER in our system, we wondered if our approach could be used to more finely quantify the effect of other sources of viscous drag. The Stokes–Einstein formula predicts that the mean diffusion coefficient of freely diffusing molecules should be inversely proportional to the radius of the molecule. We tested our ability to resolve this relationship by generating a larger version of a free-floating molecule in the ER lumen. Briefly, we genetically fused a signal sequence to three codon optimized concatemers of the HaloTag linked by flexible linkers and C-terminally fused to a KDEL retention sequence (3×HaloTag–KDEL).

As predicted for a system dominated by diffusional mobility, the photoactivated 3×HaloTag–KDEL explored a slightly smaller proportion of the cell in a defined time window than the single HaloTag–KDEL construct (compare, for example, fig. 5A with fig. 4B). Although a few cells did show some degree of anisotropy in arrival times of fluorescent molecules, the majority of the data fit well to an isotropic model. Again, we found that the dispersion of the 3×HaloTag was most effectively fit with a model for simple Brownian motion (effective MSD exponent $\alpha_{3\times}$=1.01, fig. 5B–C). (fig. 5A). However, in agreement with physical characteristics of diffusion, we observed decreased mixing speed for the 3×HaloTag–KDEL compared to single HaloTag–KDEL ($D_{3\times}$ = 8.53 μm^2 s^{-1}, $D_{1\times}$ = 16.84 μm^2 s^{-1}, p-value < 1 × 10^{-3}, see fig. 5D). Notably, as a control, the same 3×HaloTag fused to the transmembrane targeting domain of Sec61β had no statistically significant effect on its diffusion characteristics, since the viscous drag of the membrane on the membrane anchor is dominating (fig. 5C–D).

E. Dynamics of misfolded proteins in the ER lumen

One of the major functions of the ER is to serve as the major site of translation, folding, and quality control for membrane and secreted proteins [50, 51]. Studies using FRAP have demonstrated that during homeostasis the binding events of unfolded proteins to ER chaperones are transient and manifest as a slowed effective diffusion coefficient [59]. However, if proteins are damaged or misfolded for too long, they can be removed from the ER and degraded through a process known as ERAD [51]. Studies with FRAP have suggested that under these conditions, proteins may become effectively immobilized [31, 56]. Since our approach can accurately discern the small differences associated with protein size and provides a spatial-dependent estimate of diffusion that is not achievable with FRAP, we sought to try to observe how a misfolded protein would work in our system.

To this aim, we took advantage of the fact that the protein CD3δ is obligately misfolded and degraded in normal tissue culture cells [6, 8]. Truncation experiments have shown that luminal domain alone is sufficient for misfolding and degradation when expressed as a soluble construct [6, 39]. We fused the signal sequence and soluble domain of CD3δ to HaloTag (CD3δΔ–HaloTag) to generate a photoactivatable version of a model misfolded protein. We then performed our full analysis pipeline, and analysed the dispersion of CD3δΔ–HaloTag from the PA source.

Examination of cells expressing the misfolded construct showed that a significant fraction of the protein was still dynamic within the system, allowing us to perform the full analysis pipeline (fig. 6A). Like the other constructs, most of the CD3δΔ–HaloTag-expressing cells fit well with an isotropic model. However, when analysed as a function of distance from the PA source, many CD3δΔ–HaloTag-expressing cells showed a trend towards higher diffusion at distances further away from the PA source (fig. 6B, see Discussion).

The mean effective diffusion coefficient is significantly reduced for the misfolded protein ($D_{\text{CD3}\delta\Delta}$ = 6.19 μm^2 s^{-1}, D_{KDEL} = 16.84 μm^2 s^{-1}, p-value < 1 × 10^{-3}, see fig. 6D). Since this is predicted for a protein interacting with ER luminal chaperones, our data is consistent with that shown by FRAP [59].

III. DISCUSSION

In this article, we have combined high speed imaging with point-based photoactivation to examine the dynamic properties of proteins within the ER network. We have combined this with a machine learning-based segmentation pipeline and a spatially-defined model fitting procedure that can extract quantitative information about motion within the ER network, based on knowledge of the organelle morphology obtained by simultaneous acquisition of a GFP channel labelling the ER structure. We have shown how taking into account the ER morphology can significantly change the interpretation of the molecules dynamics (fig. 1). In particular, we highlighted how large-scale superdiffusive behaviour can emerge when the analysis is limited to the photoactivatable channel, but the same data can be well explained by an effective diffusion model when the morphology of the network is considered. By blending a simulation of purely diffusive model to the ER morphology measured from the GFP-labeled channel, we have shown that we can qualitatively reproduce the heterogeneity of the photoactivatable channel (fig. 2). Our results suggest that brighter regions in the photoactivatable channel are not necessarily associated to protein accumulation or heterogeneous mixing, but may be a result

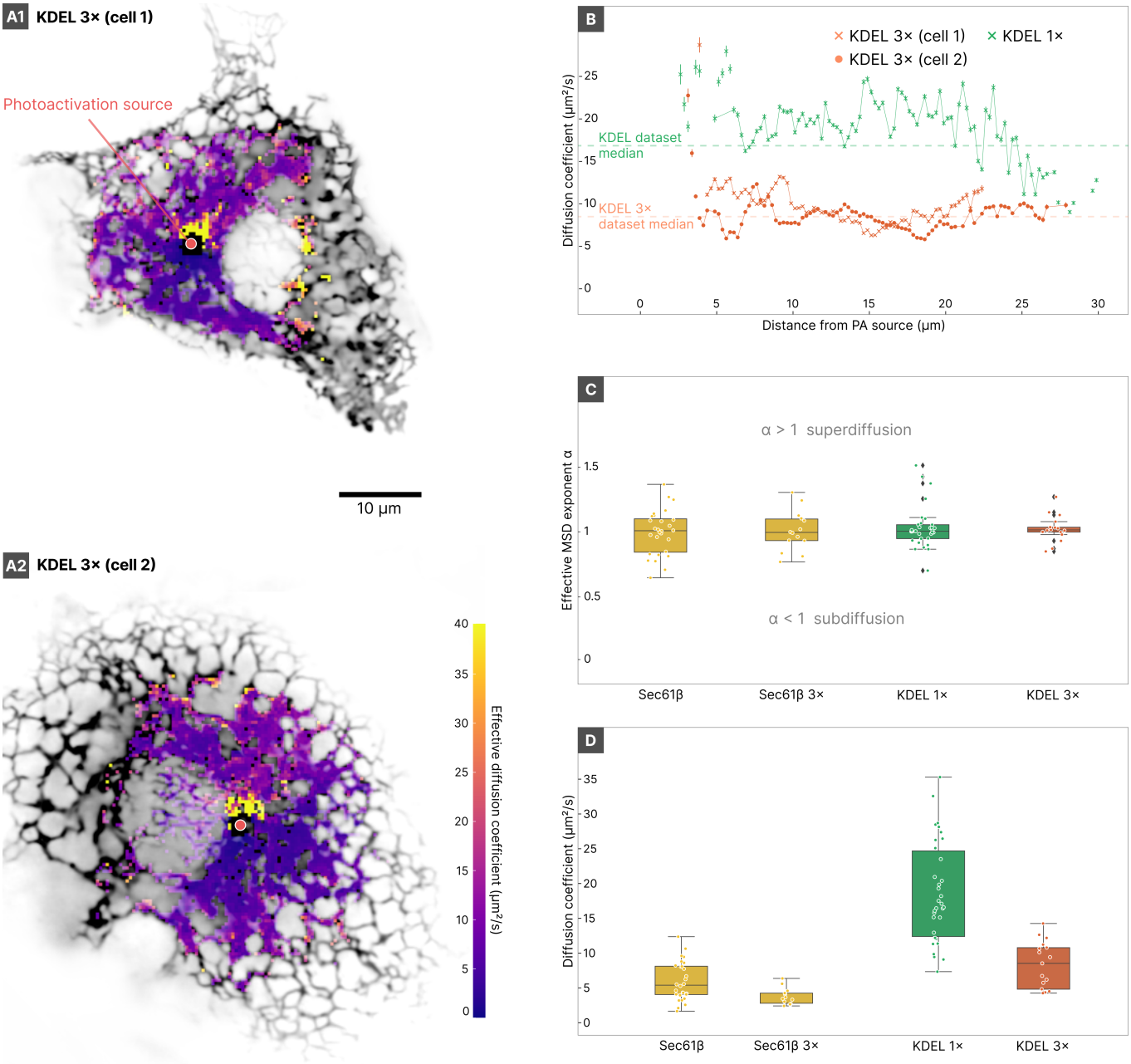

Figure 5. **Diffusion in the ER lumen but not the membrane is protein size-dependent.** **A** Examples of spatial diffusion map for cells of 3×HaloTag–KDEL. **B** Results for the isotropic diffusion fit (average over all targets at fixed distance) for the cells shown in A1 and A2 (3×HaloTag–KDEL), compared to an example of HaloTag–KDEL. **C** Population statistics of the effective MSD exponent of for HaloTag–Sec61β, 3×HaloTag–Sec61β (control), HaloTag–KDEL, and 3×HaloTag–KDEL. **D** Population statistics of the effective diffusion coefficient D_{eff} for the same conditions.

of higher structural density of the ER. To discern whether heterogeneities observed in the photoactivated signal derive from a variation of structure density or are actual signs of uneven protein redistribution, the photoactivatable channel should be systematically compared with the underlying organelle geometry.

Despite the evidence we have previously presented supporting locally directed motion of ER luminal proteins using SPT [27], we were unable to detect any evidence in this study supporting the active-flow network model (AFN) introduced in [13]. We can think of three potential sources for this inconsistency. First, the spatial and time scales of locally-directed luminal flows are still a subject of some debate, but they may exist over scales that are beneath the resolving power of spinning disk microscopy as we have implemented it here. Thus, they are only observed in SPT-based approaches. In this sense the results we report here are coherent with the AFN model, which is known to become equivalent to effect-

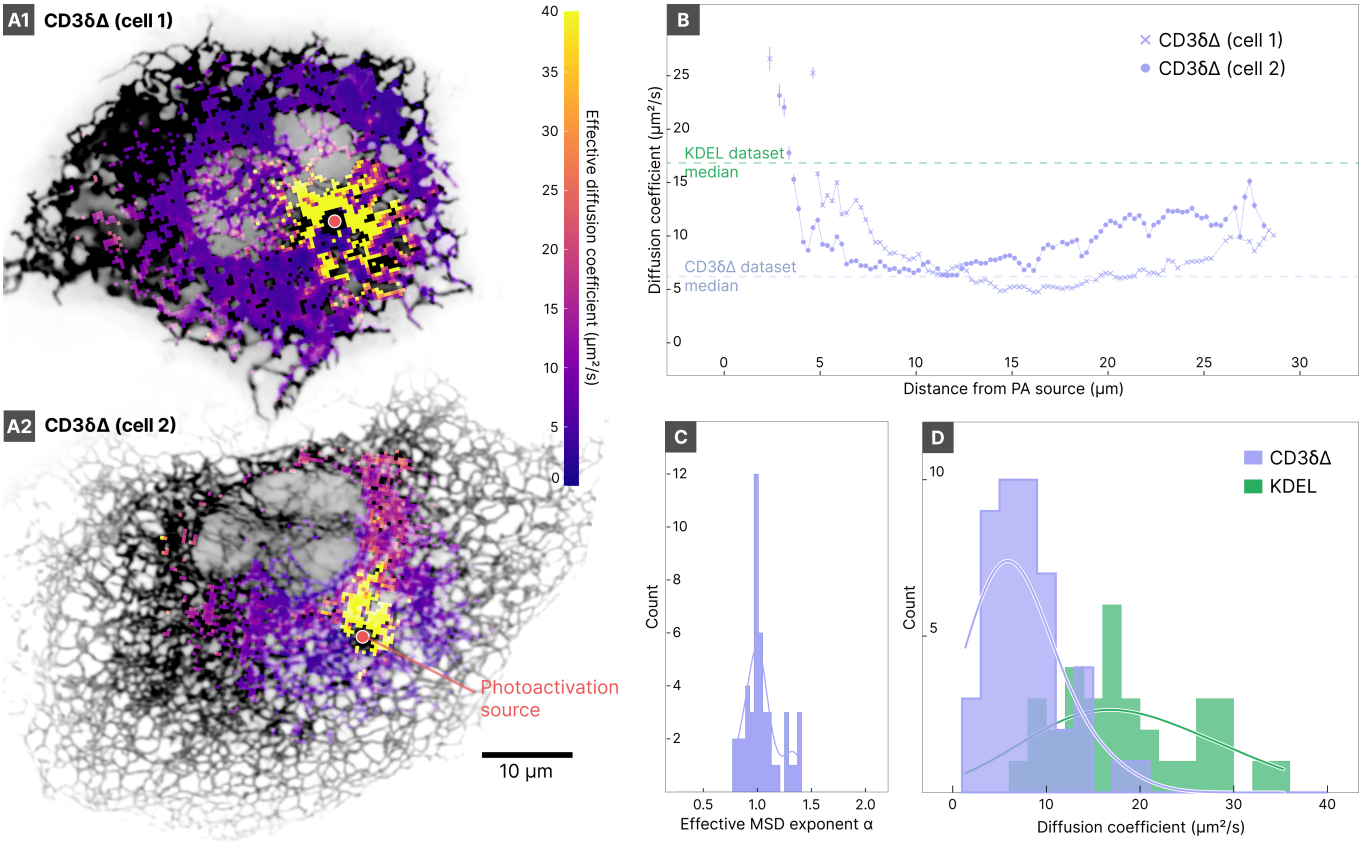

Figure 6. **Misfolded luminal proteins show slowed effective diffusion and confined motion.** **A** Representative examples of spatially defined diffusion of CD3δΔ–HaloTag. **B** Isotropic diffusion fit for the cells shown in A1 and A2 (CD3δΔ–HaloTag). **C** Distribution of the effective MSD exponent for the CD3δΔ–HaloTag condition. **D** Distribution of effective diffusion coefficient D_{eff} for CD3δΔ–HaloTag (lavender), compared to HaloTag–KDEL condition.

ive diffusion when the network operates at timescales much smaller than the observation interval [13]. Second, SPT is currently only able to be used at the outer periphery of cells, where our spatially defined model approach is the least robust. It may be that we could not observe a significant contribution of the ER flow to our data because it is simply not present in enough of the structure to be detected when averaging. Third, ER flows are not universal or only occur in some situations. Either way, resolving this issue will require more data collected by both SPT and our approach, ideally in the same system simultaneously. This will be an attempted target of future work.

Another surprising observation made in this study is that in some cells, there is significant anisotropy in the arrival times of fluorescent proteins. This was true to some extent for all the conditions, though it was always a small fraction of the total cells. In general, poor model fitting of this nature might be a predicted result of non-diffusive motion, but there are a few reasons we do not feel this is the most parsimonious explanation in this circumstance. First, these cells do not have effective MSD exponent fits that are significantly greater than 1, as would be predicted if such significant regions of the cell were undergoing directed motion. Second, the location of the regions is almost always in the perinuclear region immediately juxtaposed to the nuclear envelope. This region of ER in tissue culture cells is astoundingly structurally complex and cannot be resolved by light microscopy [25, 45, 68]. Thus, it may be that in these complex regions our segmentation becomes a poor predictor of actual connectivity. Either way, it suggests that the ER of cells is not guaranteed to be evenly connected, which may carry important implications for many biological sorting processes. A search for proteins that may affect this connectivity will be a focus of future work.

Although it was not universal, many cells showed a slight upwards trend in effective diffusion coefficient at distances quite far from the PA source. This was notable in the CD3δΔ examples shown in fig. 6, but was present in some cells in each of the other conditions as well. We do not have a clear explanation for this phenomenon, but one possibility is that, as we increase the distance from the PA source (which was nearly always placed in the dense central regions of the cell) and go towards the ER periphery, the connectivity is reduced, making the 2D effective diffusion model inexact as the dimensionality gets closer to 1 (e.g. for the case of a molecule moving along a single tubule). Moreover, there is building data that ER tubules at the extreme periphery can be very thin [62, 67]. As the tubes get narrower, they may funnel mo-

lecules more efficiently to the end than in thicker tubes with more space for lateral motion. This will be an interesting direction for SPT experiments in the future.

It is an interesting result of this study that the fusion of the small misfolded domain of CD3δΔ slows effective HaloTag diffusion by a similar effect to that of linking three HaloTags as concatemers. A weakness of our ensemble approach to analysing diffusion is that a molecule with multiple distinct forms only reports the average of these states. It is impossible to say from this data what proportion of the molecules are in confined states in any given cell, but future experiments combining SPT or carefully designed drug treatments may be able to parse the contributions of chaperone binding from degradation-associated confinement in the net slowing of the CD3δΔ dispersal.

In conclusion, in this work we have developed a quantitative approach to monitor high-speed protein dynamics within the ER, taking into account the organelle geometry. We see that, when the ER morphology is considered, proteins in the lumen and the membrane are largely governed by bulk diffusion, although their dynamics is not always spatially homogeneous. With our method, we could produce quantitative measures of how different aspects of membrane topology and size affect molecular motion.

IV. METHODS

Fluorescence microscopy images are acquired in low-light conditions, since the power of the excitation laser and exposure interval are constrained by the fluorescence saturation rate, the risk of photodamaging the sample, and the acquisition rate for dynamical imaging. Fluorescent images are thus characterized by high level of noise. In particular, the main source of disturbance is represented by Poisson noise (or *shot noise*) originating from the discrete number of photons hitting the sensor [18]. This is combined with other signal-independent noise sources, due to thermal vibration (e.g. dark current) or caused by the electronics (i.e. noise due to the amplification, conversion, and transmission process, which is usually collectively indicated as *readout noise*). These last noise sources do not depend on the photon flux, and can be modelled effectively as a single aggregated white noise source. Thus, denoising of fluorescence images requires handling Poisson-Gaussian noise. Various techniques have been developed to solve this problem, following mainly three approaches: variance stabilizing transformation followed by additive white noise removal [18], algorithms specifically designed for Poisson-Gaussian mixtures such as PURE-LET [37], and deep learning models based on CNN [32, 69]. A recent work, benchmarking the most popular methods on a dataset of fluorescence images, highlighted the superior performances of CNN-based models [71]. The main drawback of CNN is that they usually require training on a set comprising both noisy and clean images. However, in the last few years various deep learning models have been proposed which allow training without clean data [4, 32, 65]. Another drawback of CNNs is the phenomenon of pareidolia, i.e. the tendency to impose a meaningful interpretation to random or ambiguous patterns. CNN are, by their nature, biased towards certain structures which can be intrinsic or derived from the training data [40, 65]. While this is the very reason of their effectiveness, it can also be the cause of unwanted visual artefacts: a CNN model trained on ER images will develop a tendency to see ER even where there is none. For these reasons, in our analysis of photoactivation data, we have taken a mixed approach: we relied on a deep-learning model to facilitate the segmentation of the ER morphology, but followed a more conservative approach when extracting quantitative measures from the photoactivation curves, considering a statistical model of the raw data.

A. Pre-processing and segmentation of ER morphology

To ensure reliable segmentation of the ER structure, we preprocess the data of the morphology channel (GFP channel) in several steps (see supplementary fig. S1). These preprocessing steps are needed because the ER structure and density can vary significantly. Regions of the ER close to the nuclear envelope are characterized by denser structures (membrane sheets or dense matrices of tubules [45, 63]) which are not resolvable with confocal microscopy and thus appear as continuous membrane arrangements. At the cell periphery, the ER is formed by a network of sparse tubules with diameter 60–100 nm [45, 57]. These structural differences determine the quantity of fluorescent proteins and worsen the image contrast, making it challenging to segment simultaneously the entire ER structure [47].

1. *Frame denoising*

We first denoised the morphology data to reduce the level of noise and improve the detection of finer structures. To this aim, we adapted the Noise2Noise technique [32] to train a U-Net convolutional neural network [52] for noise removal of single frames (see supplementary fig. S1A). We trained U-Net model using pairs of noisy realizations generated by extracting 128×128 px tiles from time-adjacent frames. One noisy realization is kept as a reference while the other is processed by the U-Net model. The loss is then calculated as the MSE between the reference noisy frame and the model output. This approach relies on the assumption that the acquisition rate is fast enough to make changes between consecutive frames negligible. The assumption is reasonable as most of the ER structure is steady for the acquisition interval used (100 ms). To minimize the bias created by the time evolution of the ER network, both the order of the training samples and the order of the two images forming a couple were randomized in the repeated training epochs. We kept 10% of the samples for validation, separating them from training data. The training was performed on batches of 4 images, using the Adam optimization algorithm [30] with parameters $\beta_1 = 0.9$, $\beta_2 = 0.99$, no weight decay and initial learning rate $\gamma = 2.75 \times 10^{-4}$. The learning rate was then gradually

reduced with a factor 0.75 when the MSE loss calculated on the validation set did not improve over 5 epochs. To prevent overfitting, training was stopped when the loss over the validation set did not improve for 15 consecutive epochs, selecting the model with minimal loss.

2. *Sharpening and structure enhancement*

To enhance the resolution of the finer ER structure, we deconvolved the morphology frames to create sharper images. Image deconvolution is an inverse problem of the type $\boldsymbol{y} = \mathbf{A}\boldsymbol{x}$, consisting in recovering the sharp image $\boldsymbol{x}$ from a blurred version $\boldsymbol{y}$, with $\mathbf{A}$ representing the PSF operator associated to the optical system. Since the problem is ill-posed, the solution is found by adding regularization constraints on $\boldsymbol{x}$ such as total variation [19]. Recently, a sparsity constraint in the deconvolution procedure has been shown to successfully increase the spatio-temporal resolution in fluorescence microscopy [72]. Based on these approaches, we defined a spatio-temporal deconvolution problem with total variation and sparsity regularization terms, to provide good reconstruction of edges, and a smoothness constraint in time dimension to account the gradual structural movements. We define the optimization problem as

$$\begin{aligned}\arg\min_{x}\Big(&\frac{\mu}{2}\|\boldsymbol{y}-\mathbf{A}\boldsymbol{x}\|_2^2+\lambda_t\|\boldsymbol{x}\|_1\\&+\lambda_v\sum_{n=1}^{N}\|\nabla_{\boldsymbol{v}_n}\boldsymbol{x}\|_1+\lambda_2\|\nabla_t^2\boldsymbol{x}\|_1\Big)\end{aligned} \tag{1}$$

where y represents a sequence of frames, A is the PSF operator, $\|\cdot\|_1$ and $\|\cdot\|_2^2$ represent respectively the ℓ_1 and ℓ_2 norms, $\nabla_{\boldsymbol{v}_n}$ is the directional derivative along $\boldsymbol{v}_n$, and ∇_t^2 is the second derivative in the time dimension. Multiple spatial directions $\boldsymbol{v}_n = (\sin(2\pi n/N), \cos(2\pi n/N), 0)$ in space (x, y, t) to reduce staircase artefacts. To ensure correct enforcement of the sparsity constraint, each frame in $\boldsymbol{y}$ was preprocessed by taking a 2D discrete wavelet transform and dampening the approximation coefficients by a factor 0.5. The operator A was assumed to be a Gaussian PSF with appropriate standard deviation (1.27 px). The solution $\boldsymbol{x}$ was computed with the split Bregman method [20]. Parameter values used in the optimization are reported in supplementary table S1.

3. *Segmentation of the network structure*

The ER network was segmented from the sharpened stack as follows. First, the frames were clipped at zero and rescaled between 0 and 1 and local contrast was enhanced by contrast limited adaptive histogram equalization (CLAHE) [1] for five iterations. To detect tubular structures, the frames were first transformed with a Sato tubeness filter [53] with $\sigma = 100$ nm and then binarized by locally adaptive Niblack thresholding [43] with window size 127 px ($\approx$ 17 µm) and weight 0.1. Empty background regions, which could create bad detections with purely local thresholding, were excluded by setting a minimum global threshold. Continuous surfaces corresponding to dense matrices and cisternæ were obtained by a similar thresholding procedure, followed by a morphological opening operation with a disk of radius 250 nm. The thresholded tubules and sheets were then merged in a single frame sequence. To preserve details in very close tubular structure, local minima were identified with a h-minimum transform (with threshold 1×10^{-3}) before and set to zero [47]. To fix occasional flickering of isolated pixels, a morphological closing operation was applied along the time axis of the thresholded stack. Finally, the network structure was extracted by thinning procedure [70]. To preserve dense matrices and cisternæ, these regions were again extracted by morphological opening and added back to the skeletonized network structure.

B. Estimation of morphology reshaping

The amount of local morphological reshaping was quantified in two ways. First, by estimating the relative variance of the denoised morphology frames along the time stack, highlighting regions of the network undergoing more variation in time. Predictably, most of the variation was localized on the tubule edges, due to small oscillations (fig. S2B, blue shade). Note that in our method, such small oscillations do not affect the estimate of the dynamics, as only the pixels clearly belonging to the ER structure are considered. Second, we estimated motion of tubules and other structures by optical flow using Farnebäck's algorithm [16], then calculated the mean norm of the velocity vectors over the photoactivation time to reveal regions characterized by more active reshaping of the network structure (fig. S2B, red shade).

C. Statistical model of the photoactivatable channel

1. *Estimation of the noise model parameters*

We considered a Poisson-Gaussian noise model with clipping as described in [17, 18]. The original unclipped noise model which describes the observed pixel value $z(x)$ at position x is defined by

$$\begin{aligned} z(x) &= y(x) + \sigma(y(x))\,\xi(x)\\ \sigma^2(x) &= a\,y(x) + b \end{aligned} \tag{2}$$

where $y(x)$ is the true pixel value, $\xi(x)$ is zero-mean and unit variance random noise, and $\sigma(y)$ is the y-dependent standard deviation function characterizing the Poisson-Gaussian noise. Note that this model assumes that the photon count y is large enough, such that the Poisson term can be approximated with a normally distributed noise with signal-dependent variance. Imaging sensors are also characterized by a bias level μ, i.e. an artificial offset added to the collected charge to reduce clipping. This offset value must be subtracted from the readout to correctly model the signal-dependent part of the noise, e.g. by considering the variance function $\sigma(y-\mu)$

or by redefining $y \leftarrow y - \mu$. If the sensor is not able to capture the full dynamic range of the image (particularly in the case of fluorescence imaging, where frames are intrinsically underexposed), one can define a clipped observation model as:

$$z_c(x) = \max\{0, \min\{z(x), 1\}\}. \tag{3}$$

The goal is to reconstruct the model parameters $a, b,$ from the video data. We applied the technique described in [18] on all frames, segmenting the full video data in level sets, excluding the tubules boundaries obtained from the segmentation of the morphology channel, to estimate $(\hat{y}_i, \hat{\sigma}_i)$ pairs. We then performed a maximum likelihood fit of the model parameters using the L-BFGS algorithm [41, 74].

2. *Effective diffusion model*

To extract quantitative features describing the protein dynamics, we consider an effective 2D diffusion model. The approximation with a 2D space is appropriate given that the ER structure in COS-7 cells can, for most of its surface, described by a planar graph [45]. While it is possible to derive a reaction-diffusion system which modelling a constant-rate photoconversion in the source ROI, this approach requires knowledge (or fit) of the photoconversion rate parameter. Moreover, due to the reshaping of the ER, the ROI exposed to the photoactivation laser may change constantly, altering the effectiveness of photoconversion. To avoid these problems, we used a hybrid approach which allows to preemptively tune the diffusion model based on the data. To this aim, we considered a diffusion model in which we impose a time-dependent Dirichlet boundary condition corresponding to the fluorescence measured close to the photoactivation ROI. We denote by $\phi(t)$ the protein concentration measured at distance R from the centre of the photoactivation ROI. Given an analytical expression for $\phi(t)$, we can calculate the solution of the radial diffusion equation $u(r,t)$ (see supplementary IV D, eq. S8):

$$u(r,t) = \int_0^t \mathrm{d}\tau\, \phi(t-\tau)\, \partial_t v(r,t), \tag{4}$$

where $v(r,t)$ is the solution of the auxiliary diffusion problem with a constant boundary condition ($\phi(t) = 1$), which can be explicitly expressed in Laplace domain as

$$\hat{v}(r,s) = \frac{K_0(\sqrt{\frac{s}{D}}\, r)}{s\, K_0(\sqrt{\frac{s}{D}}\, R)}, \tag{5}$$

where K_0 is the modified Bessel function of order zero. It is convenient to express the convolution in eq. (4) as a product in the Laplace domain:

$$\hat{u}(r,s) = \hat{\phi}(s)\, \frac{K_0(\sqrt{\frac{s}{D}}\, r)}{K_0(\sqrt{\frac{s}{D}}\, R)}, \tag{6}$$

calculating the $u(r,t)$ by inverting the Laplace transformation.

In principle, we can choose any analytical form of $\phi(t)$ that well describes the fluorescence curve at distance R from the centre of the photoactivation ROI observed in the experimental data. We considered here the particular case where $\phi(t)$ can be expressed as a sum of exponentially saturating functions:

$$\phi(t) = \sum_n c_n \left(1 - e^{-\lambda_n t}\right), \tag{7}$$

$$\hat{\phi}(s) = \sum_n c_n \left(\frac{1}{s} - \frac{1}{s+\lambda_n}\right). \tag{8}$$

Using this definition for ϕ combined with eq. 6 we can write

$$\hat{u}(r,s) = \sum_n c_n \left(\frac{1}{s} - \frac{1}{s+\lambda_n}\right) \frac{K_0(\sqrt{\frac{s}{\alpha}}\, r)}{K_0(\sqrt{\frac{s}{\alpha}}\, a)}, \tag{9}$$

from which $u(r,t)$ can be obtained by inverting the Laplace transform numerically.

3. *Fluorescence intensity model*

To properly describe the fluorescence data, we need to take into account variations which not related to the diffusion process. These are mainly constituted by the background intensity and the random photoconversion of proteins outside the photoactivation region due to leaks from the other channel and acquisition laser. We describe these by an offset and a linear trend which can be observed before the photoactivation laser is activated. Thus, we describe the fluorescence intensity $f(\boldsymbol{x}, t)$ at position $\boldsymbol{x}$ as the sum of a linear polynomial $c_1\, t + c_0$ and the diffusion process $u(r,t)$:

$$f(\boldsymbol{x}, t) = c_2(\boldsymbol{x})\, u(|\boldsymbol{x} - \boldsymbol{x}_0|, t) + c_1(\boldsymbol{x})\, t + c_0(\boldsymbol{x}) \tag{10}$$

where x_0 is the location of the PA ROI, $c_0(\boldsymbol{x})$ describes the background luminosity, $c_1(\boldsymbol{x})$ is the slope of the linear trend of random photoactivation, and $c_2(\boldsymbol{x})$ is a proportionality constant representing the density of photoactivated proteins. Note that, in general, the coefficients $c_0, c_1,$ and c_2 are space-dependent.

4. *Maximum-likelihood fit of the diffusion model*

We first performed image registration on the photoactivation channel to match the position of the GFP channel by cross-correlation [3, 23]. We then considered the intensity data obtained from the raw images in the form of points $x_i = (r_i, z_i, t_i)$, where r_i represents the distance from the photoactivation source and z_i its measured fluorescence at time t_i from the beginning of photoactivation. We used the noise model defined in eq. (2), with parameters determined according to the procedure described above, to estimate the likelihood of the fluorescence model of eq. (10) depending on the x_i samples. The noise variance for a point $x_i = (r_i, z_i, t_i)$ is given by

$$\sigma_i^2 = a\, \left(f(r_i, t_i) - \mu\right) + b, \tag{11}$$

where $f(r_i, t_i)$ is the true fluorescence value and μ is the imaging sensor bias level. We consider $z_i \sim \mathcal{N}(f(r_i, t_i), \sigma_i^2)$. The log-likelihood is then

$$\log \mathcal{L}(\theta) = -\frac{1}{2} \sum_i \left(\log \left(2\pi\sigma_i^2\right) + \frac{\left(z_i - f(r_i, t_i; \theta)\right)^2}{\sigma_i^2} \right) \tag{12}$$

with θ is the set of parameters c_0, c_1, c_2, D (see eq. (10)). The maximum likelihood parameter is obtained as

$$\hat{\theta} = \arg\max_{\theta} \log \mathcal{L}(\theta), \tag{13}$$

which can be solved by numerical optimization. This maximum likelihood estimation can be extended to ensemble points obtained by averaging multiple pixel values in the photoactivation stack. The noise variance of such aggregated points is simply

$$\hat{\sigma}_i^2 = \frac{a\left(\tilde{z}_i - \mu\right) + b}{N}, \tag{14}$$

where N is the number of averaged pixels and $\tilde{z}_i$ is average fluorescence value. By maximum-likelihood estimation it is then possible to recover the diffusion coefficient D and the coefficients $\tilde{c}_0, \tilde{c}_1$, and $\tilde{c}_2$ corresponding respectively to the average background intensity, average slope of the linear trend, and average density over the ensemble. In practice, we fit the model parameters using L-BFGS-B [41, 74] in two separate steps. First we performed the maximum likelihood fit on the interval preceding photoactivation, recovering the trend parameters c_1 and c_0. Then, fixing c_1 and c_0, we performed the fit on the full time interval to recover D and c_2. We initialized the parameter c_2 based on the GFP-labeled morphology channel as follows. We considered the frames of the morphology channel preceding photoactivation and calculate the average intensities $\rho_\mathrm{s}, \rho_\mathrm{t}$ and variances $\nu_\mathrm{s}^2, \nu_\mathrm{t}^2$ over the pixels corresponding to the PA source and the target regions respectively. We then defined the initial value for coefficient c_2 as:

$$c_2^{(\mathrm{ini})} = \frac{\rho_\mathrm{t} - \mu_\mathrm{GFP}}{\rho_\mathrm{s} - \mu_\mathrm{GFP}}, \tag{15}$$

where μ_GFP is the sensor bias level for the GFP channel. In the morphology-aware approach, we constrained the coefficient c_2 in the interval $c_2^{(\mathrm{ini})} \pm 5\nu$, where ν^2 is the approximated variance of the ratio distribution obtained as $\frac{\rho_\mathrm{t}^2}{\rho_\mathrm{s}^2}\left(\frac{\nu_\mathrm{t}^2}{(\rho_\mathrm{t}-\mu_\mathrm{GFP})^2} + \frac{\nu_\mathrm{s}^2}{(\rho_\mathrm{s}-\mu_\mathrm{GFP})^2}\right)$.

In the case of isotropic diffusion estimation, these ensemble points were built by binning pixels in each frame based on their distance from the PA source (with bin size of 250 nm). Only pixels belonging to the segmented ER structure were considered. Ensemble points characterized by the same distance r were grouped to build a time series $(r, \tilde{z}_i, t_i)_{i=1,2,\ldots}$. We note that, due to changes in the morphology of the ER, the pixels belonging to a given distance bin are not invariant across frames. This frame by frame adjustment allows cancelling at least part of the effect of the morphology reshaping.

For the estimation of space-dependent effective diffusion, ensemble points were built by dividing the field of view in equal bins using a squared grid (fig. 3A). For each bin, average fluorescence intensity and median distance from the source were evaluated in each frame (considering only the pixels belonging to the segmented ER structure, fig. 3B). The ensemble points obtained by this procedure were then used to estimate the effective diffusion by maximum likelihood (fig. 3C), obtaining a diffusion coefficient for each bin of the grid (fig. 3D).

We estimated the variance of the fitted parameter D using the observed Fisher information. In the limit of large number of samples, the distribution of the maximum likelihood estimate $\hat{\theta}$ can be approximated as [24]:

$$\hat{\theta} \sim \mathcal{N}\left(\hat{\theta}, I(\hat{\theta})^{-1}\right), \tag{16}$$

where $I(\hat{\theta})$ is the observed Fisher information. In our case, the observed Fisher information can be evaluated as the Hessian of the negative log-likelihood defined in eq. (12), i.e. $I(\hat{\theta}) = H\left(-\log \mathcal{L}(\theta)\right)|_{\hat{\theta}}$. We thus estimated the variance of the parameter D by numerically evaluating the inverse Hessian of $-\log \mathcal{L}$ at its minimum [9], and taking the appropriate diagonal element. We note that such estimate of the error is statistically meaningful only limited to the context of the optimization problem defined in eq. (13), as it does not take into account errors resulting from inappropriateness of the effective diffusion model or bad ER segmentation. Nevertheless, this approach provides a method to systematically rate the quality of the fits and exclude the unreliable datapoints in the estimation of the effective diffusion coefficient (fig. 1C).

[1] The Graphics Gems Series. In Paul S. Heckbert, editor, *Graphics Gems*, page ii. Academic Press.

[2] Bastian R Angermann, Frederick Klauschen, Alex D Garcia, Thorsten Prustel, Fengkai Zhang, Ronald N Germain, and Martin Meier-Schellersheim. Computational modeling of cellular signaling processes embedded into dynamic spatial contexts. *Nature methods*, 9(3):283–289, 2012.

[3] Paul E Anuta. Spatial registration of multispectral and multitemporal digital imagery using fast fourier transform techniques. *IEEE transactions on Geoscience Electronics*, 8(4):353–368, 1970.

[4] Joshua Batson and Loic Royer. Noise2Self: Blind denoising by self-supervision. In *International Conference on Machine Learning*, pages 524–533.

[5] Buzz Baum and David A Baum. The merger that made us. *BMC biology*, 18(1):1–4, 2020.

[6] Riccardo Bernasconi, Carmela Galli, Verena Calanca, Toshihiro Nakajima, and Maurizio Molinari. Stringent requirement for

hrd1, sel1l, and os-9/xtp3-b for disposal of erad-ls substrates. *Journal of Cell Biology*, 188(2):223–235, 2010.

[7] Michael J Berridge. The endoplasmic reticulum: a multifunctional signaling organelle. *Cell calcium*, 32(5-6):235–249, 2002.

[8] Juan S Bonifacino, Carolyn K Suzuki, Jennifer Lippincott-Schwartz, Allan M Weissman, and Richard D Klausner. Pregolgi degradation of newly synthesized t-cell antigen receptor chains: intrinsic sensitivity and the role of subunit assembly. *The Journal of cell biology*, 109(1):73–83, 1989.

[9] Per A. Brodtkorb and John D'Errico. numdifftools. `https://github.com/pbrod/numdifftools`, 2015.

[10] Nelson B Cole, Carolyn L Smith, Noah Sciaky, Mark Terasaki, Michael Edidin, and Jennifer Lippincott-Schwartz. Diffusional mobility of golgi proteins in membranes of living cells. *Science*, 273(5276):797–801, 1996.

[11] Lindsey M Costantini, Mikhail Baloban, Michele L Markwardt, Megan A Rizzo, Feng Guo, Vladislav V Verkhusha, and Erik L Snapp. A palette of fluorescent proteins optimized for diverse cellular environments. *Nature communications*, 6(1):1–13, 2015.

[12] Lindsey M Costantini and Erik Lee Snapp. Fluorescent proteins in cellular organelles: serious pitfalls and some solutions. *DNA and cell biology*, 32(11):622–627, 2013.

[13] M Dora and D Holcman. Active flow network generates molecular transport by packets: case of the endoplasmic reticulum. *Proceedings of the Royal Society B*, 287(1930):20200493, 2020.

[14] Jan Ellenberg, Jennifer Lippincott-Schwartz, and John F Presley. Dual-colour imaging with gfp variants. *Trends in cell biology*, 9(2):52–56, 1999.

[15] Lance P Encell, Rachel Friedman Ohana, Kris Zimmerman, Paul Otto, Gediminas Vidugiris, Monika G Wood, Georgyi V Los, Mark G McDougall, Chad Zimprich, Natasha Karassina, et al. Suppl 1: Development of a dehalogenase-based protein fusion tag capable of rapid, selective and covalent attachment to customizable ligands. *Current chemical genomics*, 6:55, 2012.

[16] Gunnar Farnebäck. Two-frame motion estimation based on polynomial expansion. In *Scandinavian conference on Image analysis*, pages 363–370. Springer, 2003.

[17] Alessandro Foi. Clipped noisy images: Heteroskedastic modeling and practical denoising. 89(12):2609–2629.

[18] Alessandro Foi, Mejdi Trimeche, Vladimir Katkovnik, and Karen Egiazarian. Practical Poissonian-Gaussian noise modeling and fitting for single-image raw-data. 17(10):1737–1754.

[19] Pascal Getreuer. Total Variation Deconvolution using Split Bregman. 2:158–174.

[20] Tom Goldstein and Stanley Osher. The Split Bregman Method for L1-Regularized Problems. 2(2):323–343.

[21] Uma Goyal and Craig Blackstone. Untangling the web: mechanisms underlying er network formation. *Biochimica et Biophysica Acta (BBA)-Molecular Cell Research*, 1833(11):2492–2498, 2013.

[22] Jonathan B Grimm, Brian P English, Heejun Choi, Anand K Muthusamy, Brian P Mehl, Peng Dong, Timothy A Brown, Jennifer Lippincott-Schwartz, Zhe Liu, Timothée Lionnet, et al. Bright photoactivatable fluorophores for single-molecule imaging. *Nature methods*, 13(12):985–988, 2016.

[23] Manuel Guizar-Sicairos, Samuel T Thurman, and James R Fienup. Efficient subpixel image registration algorithms. *Optics letters*, 33(2):156–158, 2008.

[24] Trevor Hastie, Robert Tibshirani, Jerome H Friedman, and Jerome H Friedman. *The elements of statistical learning: data mining, inference, and prediction*, volume 2. Springer, 2009.

[25] Larissa Heinrich, Davis Bennett, David Ackerman, Woohyun Park, John Bogovic, Nils Eckstein, Alyson Petruncio, Jody Clements, Song Pang, C Shan Xu, et al. Whole-cell organelle segmentation in volume electron microscopy. *Nature*, 599(7883):141–146, 2021.

[26] Koret Hirschberg, Chad M Miller, Jan Ellenberg, John F Presley, Eric D Siggia, Robert D Phair, and Jennifer Lippincott-Schwartz. Kinetic analysis of secretory protein traffic and characterization of golgi to plasma membrane transport intermediates in living cells. *The Journal of cell biology*, 143(6):1485–1503, 1998.

[27] David Holcman, Pierre Parutto, Joseph E. Chambers, Marcus Fantham, Laurence J. Young, Stefan J. Marciniak, Clemens F. Kaminski, David Ron, and Edward Avezov. Single particle trajectories reveal active endoplasmic reticulum luminal flow. 20(10):1118–1125.

[28] Maximilian AH Jakobs, Andrea Dimitracopoulos, and Kristian Franze. Kymobutler, a deep learning software for automated kymograph analysis. *Elife*, 8:e42288, 2019.

[29] Andrii A Kaberniuk, Manuel A Mohr, Vladislav V Verkhusha, and Erik Lee Snapp. moxmaple3: a photoswitchable fluorescent protein for palm and protein highlighting in oxidizing cellular environments. *Scientific reports*, 8(1):1–10, 2018.

[30] Diederik P. Kingma and Jimmy Ba. Adam: A Method for Stochastic Optimization.

[31] Chunwei Walter Lai, Joel H Otero, Linda M Hendershot, and Erik Snapp. Erdj4 protein is a soluble endoplasmic reticulum (er) dnaj family protein that interacts with er-associated degradation machinery. *Journal of Biological Chemistry*, 287(11):7969–7978, 2012.

[32] Jaakko Lehtinen, Jacob Munkberg, Jon Hasselgren, Samuli Laine, Tero Karras, Miika Aittala, and Timo Aila. Noise2Noise: Learning image restoration without clean data. volume 80 of *Proceedings of Machine Learning Research*, pages 2965–2974. PMLR.

[33] Jennifer Lippincott-Schwartz, Nihal Altan-Bonnet, and George H Patterson. Photobleaching and photoactivation: Following protein dynamics in living cells. pages S7–14.

[34] Jennifer Lippincott-Schwartz, Erik Snapp, and Anne Kenworthy. Studying protein dynamics in living cells. *Nature reviews Molecular cell biology*, 2(6):444–456, 2001.

[35] Jennifer Lippincott-Schwartz, Erik Lee Snapp, and Robert D. Phair. The Development and Enhancement of FRAP as a Key Tool for Investigating Protein Dynamics. 115(7):1146–1155.

[36] Georgyi V Los, Lance P Encell, Mark G McDougall, Danette D Hartzell, Natasha Karassina, Chad Zimprich, Monika G Wood, Randy Learish, Rachel Friedman Ohana, Marjeta Urh, et al. Halotag: a novel protein labeling technology for cell imaging and protein analysis. *ACS chemical biology*, 3(6):373–382, 2008.

[37] Florian Luisier, Thierry Blu, and Michael Unser. Image Denoising in Mixed Poisson–Gaussian Noise. 20(3):696–708.

[38] Pierre Mangeol, Bram Prevo, and Erwin JG Peterman. Kymographclear and kymographdirect: two tools for the automated quantitative analysis of molecular and cellular dynamics using kymographs. *Molecular biology of the cell*, 27(12):1948–1957, 2016.

[39] Martin Mehnert, Thomas Sommer, and Ernst Jarosch. Erad ubiquitin ligases: multifunctional tools for protein quality control and waste disposal in the endoplasmic reticulum. *Bioessays*, 32(10):905–913, 2010.

[40] Benjamin R. Mitchell. The spatial inductive bias of deep learning.

[41] José Luis Morales and Jorge Nocedal. Remark on "algorithm 778: L-bfgs-b: Fortran subroutines for large-scale bound constrained optimization". *ACM Transactions on Mathematical*

Software (TOMS), 38(1):1–4, 2011.

[42] Sarah Nehls, Erik L Snapp, Nelson B Cole, Kristien JM Zaal, Anne K Kenworthy, Theresa H Roberts, Jan Ellenberg, John F Presley, Eric Siggia, and Jennifer Lippincott-Schwartz. Dynamics and retention of misfolded proteins in native er membranes. *Nature cell biology*, 2(5):288–295, 2000.

[43] Wayne Niblack. *An Introduction to Digital Image Processing*. Strandberg Publishing Company.

[44] Benjamin J Nichols, Anne K Kenworthy, Roman S Polishchuk, Robert Lodge, Theresa H Roberts, Koret Hirschberg, Robert D Phair, and Jennifer Lippincott-Schwartz. Rapid cycling of lipid raft markers between the cell surface and golgi complex. *The Journal of cell biology*, 153(3):529–542, 2001.

[45] Jonathon Nixon-Abell, Christopher J Obara, Aubrey V Weigel, Dong Li, Wesley R Legant, C Shan Xu, H Amalia Pasolli, Kirsten Harvey, Harald F Hess, Eric Betzig, et al. Increased spatiotemporal resolution reveals highly dynamic dense tubular matrices in the peripheral ER. 354(6311):aaf3928.

[46] Bence P Ölveczky and AS Verkman. Monte carlo analysis of obstructed diffusion in three dimensions: application to molecular diffusion in organelles. *Biophysical journal*, 74(5):2722–2730, 1998.

[47] Charlotte Pain, Verena Kriechbaumer, Maike Kittelmann, Chris Hawes, and Mark Fricker. Quantitative analysis of plant ER architecture and dynamics. 10(1):984.

[48] George H Patterson and Jennifer Lippincott-Schwartz. A photoactivatable gfp for selective photolabeling of proteins and cells. *Science*, 297(5588):1873–1877, 2002.

[49] William A Prinz, Alexandre Toulmay, and Tamas Balla. The functional universe of membrane contact sites. *Nature Reviews Molecular Cell Biology*, 21(1):7–24, 2020.

[50] Tom A Rapoport, Long Li, and Eunyong Park. Structural and mechanistic insights into protein translocation. *Annual review of cell and developmental biology*, 33:369–390, 2017.

[51] David Ron and Peter Walter. Signal integration in the endoplasmic reticulum unfolded protein response. *Nature reviews Molecular cell biology*, 8(7):519–529, 2007.

[52] Olaf Ronneberger, Philipp Fischer, and Thomas Brox. U-net: Convolutional networks for biomedical image segmentation. In *Lecture Notes in Computer Science*, pages 234–241. Springer International Publishing.

[53] Yoshinobu Sato, Shin Nakajima, Nobuyuki Shiraga, Hideki Atsumi, Shigeyuki Yoshida, Thomas Koller, Guido Gerig, and Ron Kikinis. Three-dimensional multi-scale line filter for segmentation and visualization of curvilinear structures in medical images. *Medical Image Analysis*, 2(2):143–168.

[54] Ivo F Sbalzarini, Arnold Hayer, Ari Helenius, and Petros Koumoutsakos. Simulations of (an) isotropic diffusion on curved biological surfaces. *Biophysical journal*, 90(3):878–885, 2006.

[55] Ivo F Sbalzarini, Anna Mezzacasa, Ari Helenius, and Petros Koumoutsakos. Effects of organelle shape on fluorescence recovery after photobleaching. *Biophysical journal*, 89(3):1482–1492, 2005.

[56] Jingshi Shen, Erik L Snapp, Jennifer Lippincott-Schwartz, and Ron Prywes. Stable binding of atf6 to bip in the endoplasmic reticulum stress response. *Molecular and cellular biology*, 25(3):921–932, 2005.

[57] Yoko Shibata, Gia K. Voeltz, and Tom A. Rapoport. Rough sheets and smooth tubules. 126(3):435–439.

[58] Eric D Siggia, Jennifer Lippincott-Schwartz, and Stefan Bekiranov. Diffusion in inhomogeneous media: theory and simulations applied to whole cell photobleach recovery. *Biophysical journal*, 79(4):1761–1770, 2000.

[59] Erik L Snapp, Ajay Sharma, Jennifer Lippincott-Schwartz, and Ramanujan S Hegde. Monitoring chaperone engagement of substrates in the endoplasmic reticulum of live cells. 103(17):6536–6541.

[60] Yunhao Sun, Zexi Yu, Christopher Obara, Keshav Mittal, Jennifer Lippincott-Schwarz, and Elena F Koslover. Unraveling single-particle trajectories confined in tubular networks. *arXiv preprint arXiv:2112.05884*, 2021.

[61] Yunhao Sun, Zexi Yu, Christopher J. Obara, Keshav Mittal, Jennifer Lippincott-Schwarz, and Elena F. Koslover. Unraveling Single-Particle Trajectories Confined in Tubular Networks.

[62] Mark Terasaki. Axonal endoplasmic reticulum is very narrow. *Journal of Cell Science*, 131(4):jcs210450, 2018.

[63] Mark Terasaki, Lan Bo Chen, and Keigi Fujiwara. Microtubules and the endoplasmic reticulum are highly interdependent structures. 103(4):1557–1568.

[64] Roger Y Tsien. The green fluorescent protein. *Annual review of biochemistry*, 67(1):509–544, 1998.

[65] Dmitry Ulyanov, Andrea Vedaldi, and Victor Lempitsky. Deep Image Prior. pages 9446–9454.

[66] Gerrit Van Meer, Dennis R Voelker, and Gerald W Feigenson. Membrane lipids: where they are and how they behave. *Nature reviews Molecular cell biology*, 9(2):112–124, 2008.

[67] Bowen Wang, Zhiheng Zhao, Michael Xiong, Rui Yan, and Ke Xu. The endoplasmic reticulum adopts two distinct tubule forms. *bioRxiv*, 2021.

[68] C Shan Xu, Song Pang, Gleb Shtengel, Andreas Müller, Alex T Ritter, Huxley K Hoffman, Shin-ya Takemura, Zhiyuan Lu, H Amalia Pasolli, Nirmala Iyer, et al. An open-access volume electron microscopy atlas of whole cells and tissues. *Nature*, 599(7883):147–151, 2021.

[69] Kai Zhang, Wangmeng Zuo, Yunjin Chen, Deyu Meng, and Lei Zhang. Beyond a Gaussian Denoiser: Residual Learning of Deep CNN for Image Denoising. 26(7):3142–3155.

[70] Tongjie Y. Zhang and Ching Y. Suen. A fast parallel algorithm for thinning digital patterns. 27(3):236–239.

[71] Yide Zhang, Yinhao Zhu, Evan Nichols, Qingfei Wang, Siyuan Zhang, Cody Smith, and Scott Howard. A poisson-gaussian denoising dataset with real fluorescence microscopy images. In *CVPR*.

[72] Weisong Zhao, Shiqun Zhao, Liuju Li, Xiaoshuai Huang, Shijia Xing, Yulin Zhang, Guohua Qiu, Zhenqian Han, Yingxu Shang, De-en Sun, Chunyan Shan, Runlong Wu, Lusheng Gu, Shuwen Zhang, Riwang Chen, Jian Xiao, Yanquan Mo, Jianyong Wang, Wei Ji, Xing Chen, Baoquan Ding, Yanmei Liu, Heng Mao, Bao-Liang Song, Jiubin Tan, Jian Liu, Haoyu Li, and Liangyi Chen. Sparse deconvolution improves the resolution of live-cell super-resolution fluorescence microscopy. pages 1–12.

[73] H Mimi Zhou, Ingrid Brust-Mascher, and Jonathan M Scholey. Direct visualization of the movement of the monomeric axonal transport motor unc-104 along neuronal processes in livingcaenorhabditis elegans. *Journal of Neuroscience*, 21(11):3749–3755, 2001.

[74] Ciyou Zhu, Richard H Byrd, Peihuang Lu, and Jorge Nocedal. Algorithm 778: L-bfgs-b: Fortran subroutines for large-scale bound-constrained optimization. *ACM Transactions on mathematical software (TOMS)*, 23(4):550–560, 1997.